Functional Nanostructured Materials (including low-D carbon)

Laser-Deposited Carbon Aerogel Derived from Graphene Oxide Enables NO2-Selective Parts-Per-Billion Gas Sensing

Sebastian Nufer, Peter Lynch, Matthew Large, Sean P. Ogilvie, Jonathan P. Salvage, Mario Pelaez-Fernandez, Thomas Waters, Izabela Jurewicz, Edgar Muñoz, Raul Arenal, Ana M Benito, Wolfgang K Maser, Nikos Tagmatarchis, Christopher Paul Ewels, Adam Brunton, and Alan B. Dalton

ACS Appl. Mater. Interfaces, **Just Accepted Manuscript** • DOI: 10.1021/acsami.0c09112 • Publication Date (Web): 22 Jul 2020

Just Accepted

Laser-Deposited Carbon Aerogel Derived from Graphene Oxide Enables NO_2-Selective Parts-Per-Billion Sensing

Sebastian Nufer[1,2,†], Peter J. Lynch[2], Matthew J. Large[2], Sean P. Ogilvie[2], Jonathan P. Salvage[3], Mario Pelaez-Fernandez[4], Thomas Waters[5], Izabela Jurewicz[5], Edgar Muñoz[6], Raul Arenal[7,8], Ana M. Benito[6], Wolfgang K. Maser[6], Nikos Tagmatarchis[9], Christopher P. Ewels[10,], Adam Brunton[1], Alan B. Dalton[2,*]*

1 M-Solv Ltd, Oxonian Park, Langford Locks, Kidlington, Oxford, OX5 1FP, UK

2 University of Sussex, Department of Physics and Astronomy, Brighton, BN1 9RH, UK, A.B.Dalton@sussex.ac.uk

3 University of Brighton, School of Pharmacy and Biomolecular Science, Brighton, BN2 4GJ, UK

4 Instituto de Nanociencia de Aragon, Universidad de Zaragoza, Laboratorio de Microscopias Avanzadas (LMA), 50018 Zaragoza, Spain

5 University of Surrey, Department of Physics, Guildford GU2 7XH

6 Instituto de Carboquímica ICB-CSIC, 50018 Zaragoza, Spain

7 Fundacion ARAID, 50018 Zaragoza, Spain

8 Instituto de Ciencias de Materiales de Aragon, CSIC-Universidad de Zaragoza, 50009 Zaragoza, Spain

9 Theoretical and Physical Chemistry Institute, National Hellenic Research Foundation, 11635 Athens, Greece

10 Institute des Matériaux Jean Rouxel (IMN), CNRS UMR6502 / Université de Nantes, Nantes, 44322, France, Chris.Ewels@cnrs-imn.fr

KEYWORDS: Nitrogen dioxide, gas sensor, carbon aerogel, selective, chemiresistor

ABSTRACT

Laser-deposited carbon aerogel is a low-density porous network of carbon clusters synthesized using a laser process. A one-step synthesis, involving deposition and annealing, results in the formation of a thin porous conductive film which can be applied as a chemiresistor. This material is sensitive to NO_2 compared to ammonia and other volatile organic compounds and is able to detect ultra-low concentrations down to at least 10 parts-per-billion. The sensing mechanism, based on the solubility of NO_2 in the water layer adsorbed on the aerogel, increases the usability of the sensor in practically-relevant ambient environments. A

heating step, achieved in tandem with a microheater, allows the recovery to the baseline making it operable in real world environments. This, in combination with its low cost and scalable production makes it promising for Internet-of-Things air quality monitoring.

Introduction

Originating from combustion engines and industrial processes, nitrogen dioxide (NO_2) is a major air pollutant, and poses a substantial health risk causing respiratory issues which are particularly severe for asthma sufferers[1] and infants[2]. European Union regulations allow a threshold of 20 parts-per-billion (ppb) of NO_2 in the air to be overcome not more than 18 times in a year[3]. However, in London alone, the monthly average is regularly above this[4]. Recently and for the first time, doctors formally related the death of a young girl to repeated exposure to NO_2[5]. Monitoring of air quality to prevent such exposure at ppb levels is currently only possible with unwieldy, expensive equipment and is therefore scarcely implemented[6,7]. More generally, for city dwellers of tomorrow to thrive we need to overcome interdependent bottlenecks in urban infrastructure. As such, a major challenge centers on the development of highly sensitive, accurate and low-cost devices for widespread continuous monitoring of NO_2 levels in domestic, public and

industrial environments. The bottleneck to achieving high sensitivity could be addressed by materials.

Metal oxides are well established as commercially-available gas sensors capable of detecting NO_2 both at low concentration, down to 10 ppb, and with selectivity towards other harmful gases and volatile-organic-compounds (VOCs)[8]. However, these materials normally operate at elevated temperatures which would result in increased power consumption and limited operation in small-scale measurement configurations and devices. Nanomaterial structures, many carbon based, have emerged in the last decade which facilitate detection of gases at low concentration with thousand fold reduction in power consumption compared to metal oxides[9]. However, while the most promising candidates such as graphene and carbon nanotubes exhibit low limits of detection, they do not exhibit chemical selectivity in their pristine form[4,9,10]. Functionalization of the material can overcome this issue but adds a complicated synthesis step into the fabrication of devices, making manufacturing more expensive[11,12].

Here, we present a cheap, selective NO_2 sensing layer based on a laser deposited carbon aerogel (LDCA). LDCA, a porous network of amorphous carbon nanoparticles with high surface area are a well-studied structure[13]. This material is incorporated into a device structure with excellent limit of detection (close to10 ppb) produced by a scalable one-step laser deposition process,

which we analyze as a chemiresistor. Sensitivity and detection limits are determined, and several VOCs are used to ascertain the selectivity. Ultra-low limit of detection measurements demonstrates the potential of this material for adoption in Internet-of-Things type air quality monitoring devices. Measurements in different background environments establish the sensing mechanism and origin of the selectivity[14–17].

Experimental Methods

Device fabrication. IDEs (interdigitated electrodes) the substrate material used were prepared using molybdenum (700nm) on glass purchased from AimCore Technology (Hsinchu 30351, Taiwan). An MSV-101 (M-Solv Ltd, UK) laser-processing platform was used to pattern a 10mm x 10mm interdigitated electrode design using a galvanoscanner and a pulsed infrared laser (1064 nm, Multiwave, set to 150 kHz repetition rate, 10 ns pulse length) with a fluence of 3 J/cm^2 at a beam scanning speed of 1000 mm/sec. SEM of interdigitated electrode structure shown in figure S1. The same platform was then used to deposit the LDCA. The ITO (Indium Tin Oxide,) was held in place with a homemade vacuum holder. The GO, production of which is supplied in the SI along with AFM (Figure S2), Raman (Figure S3) and XPS (Figure S4), was deposited on a borosilicate glass slide (thickness

approx. 1mm) by dropcasting via pipette with no dilution and dried on hotplate. This was repeated once more to achieve suitable thickness of material. For deposition of the LDCA the GO was heated to 250°C in a ramping process of 3°/min. The Multiwave laser was set to 200 kHz resulting in 417 mJ/cm^2 with a mark-speed of 100 mm/sec. A handheld canister of dry air was used to remove the LDCA diffusion barrier by blowing.

Material characterization. Samples were imaged with a Zeiss SIGMA field emission gun scanning electron microscope (FE-SEM) using a Zeiss in-lens secondary electron detector. The FE-SEM working conditions used were 2.5 kV accelerating voltage, 20 µm aperture, and 2 mm working distance.

Samples were analyzed using a Thermo Scientific K-Alpha XPS instrument equipped with a micro-focused monochromated Al X-ray source. The source was operated at 12 keV and a 400 µm spot size. The analyzer operates at a constant analyzer energy (CAE) of 200 eV for survey scans and 50 eV for detailed scans. Charge neutralization was applied using a combined low energy / ion flood source. The spectra were deconvoluted using CASAXPS software. The XPS peaks were fitted to GL(70) line shape (a combination of 70% Gaussian and 30% Lorentzian character), after performing a Shirley background subtraction. In the fitting procedure, the FWHM (full width at half maximum) values were fixed at a maximum limit of 1.6 eV for all the peaks except the

peaks appearing at the higher energy region that tend to be much broader. Asymmetry for the sp2 carbon peak was defined as a function LA(α, β, m), where α=0.4 and β=0.38 describe the spread of the tail on each side of the Lorentzian component and the parameter m=70 specifies the width of the Gaussian used to convolute the Lorentzian curve.

Thin films were investigated using a variable-angle spectroscopic ellipsometer (J.A. Woollam Co., Inc.). Measurements were carried out with 20-nm-steps in the 400 < λ < 900 nm spectral range and for incidence angles of 50°, 60° and 70° respectively. The measurements were performed in air and at room temperature. WVASE® software version 3.888 (J. A. Woollam Co.) was used for data analysis. HRTEM imaging studies were made using an aberration-corrected FEI Titan High-Base microscope, equipped with a CEOS CETCOR Cs objective lens corrector and working at 80 kV. These works have been developed at low electron doses for avoiding potential damage and limiting charging effects.

Raman measurements were carried out using a Renishaw Invia Microscope. A 532 nm 50 mW continuous wave laser was used at 10% intensity for 10 s to produce the Raman spectrum. A total of 10 accumulations were used to enhance the signal to noise ratio.Electrochemical measurements were made using a 3 electrode

setup connected to a Gamry 600+ potentiostat. The reference electrode used as an Ag/AgCl reference and the counter electrode was a platinum wire. The electrolyte used was a 0.5 M aqueous potassium sulfate solution.

Gas measurements. A home-made gas measurement chamber was used for the measurements (see supplementary information Figure S5). Alicat mass flow controllers (programmable with maximum flow rates of 1lpm and 100sccm) were used to dilute pre-diluted NO_2 in air and nitrogen to the required concentrations. The NO_2 pre-diluted cylinders in air and in nitrogen were purchased from BOC Ltd. A LabJack was used to record the electrical data, with a set current of 1 mA. A small ceramic plate (12V 250C MCH Metal Ceramic Heater Plate Heating Element 20mm x 1.2mm) mounted to the back of the device was used to regulate the device temperature. A bubbler system consisting of tubing and a 400ml of water was connected to the mass flow controllers allowed the introduction of humid air into the system. A maximum of 30% RH was achievable due to the dry air source and the volume of the bubbler. A pre-diluted (100ppm) NH_3 in nitrogen were purchased from BOC Ltd for the exposure to ammonia. A standard calibration gas bottle was purchased for the CO_2 exposure. VOCs were added into the bubbler system and the vapor pressure was used to calculate the concentration the device was exposed to. Unless

otherwise specified sensitivity measurements were taken 15 minutes after exposure.

Results and Discussion

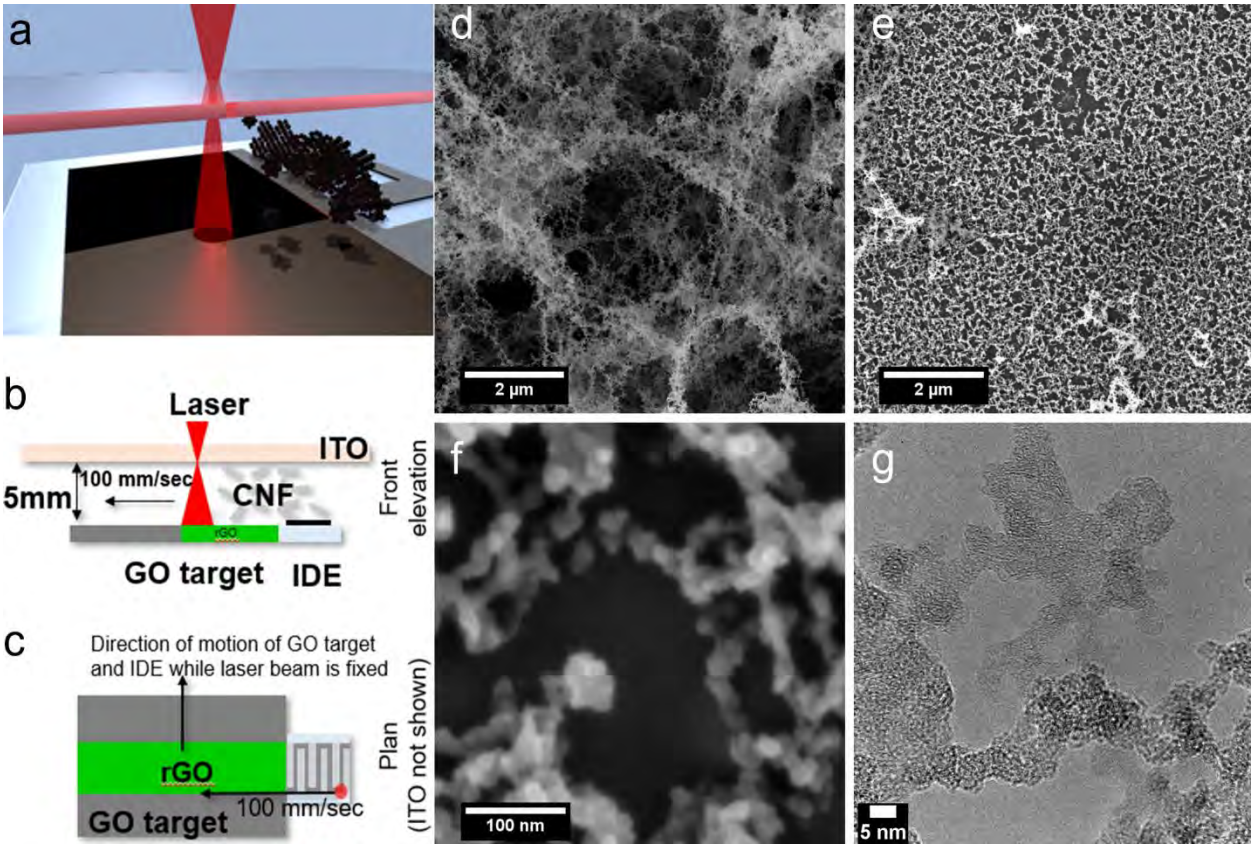

Fig1 a) Fabrication setup in 3D, b) side and c) top view of processing steps of the fabrication. SEM image of d) carbon aerogel diffusion barrier, e) active layer after removal of diffusion barrier, f) high magnifiation image of active layer, showing individual carbon clusters, g) HRTEM of LDCA diffusion barrier layer.

LDCA is an amorphous carbon nanomaterial formed when a focused laser beam interacts with a carbon target[13,18]. Carbon clusters are produced in the plasma formed above the target which subsequently diffuse to a second substrate where they aggregate, similar to the concept of pulsed laser deposition[13,19,20]. LDCA combines porosity and high specific surface area in a conductive thin film making it a promising material for high-sensitivity chemiresistive gas sensing, among other applications[13,21].

The deposition process is depicted in Figure 1a-c and further detailed in Figure S6. Interdigitated electrodes (IDE) are placed next to a graphene oxide (GO) carbon source, prepared by drop casting on borosilicate glass (see supplementary information). A transparent hydrophobic material, in our case indium tin oxide (ITO, 50Ω/sq. supplied by Aimcore) on glass, is held above the target and substrate with a airgap of 3-4mm in between. Using previously optimized conditions, an infrared laser with a constant fluence of 417 mJ/cm^2 is focused onto the ITO[13]. The laser is scanned across both the GO target and the IDE substrate (Figure 1b), which are fed perpendicular to the laser scan direction (see Figure 1c and Figure S6d). As the laser raster scans over the GO target, it produces[13] a plume of carbon and oxygen atoms leaving reduced graphene oxide (rGO)[13]. These atoms rapidly form clusters which diffuse toward the IDE substrate and are deposited to form LDCA (see SEM in Figure 1d),

guided by the ITO layer to which they do not adhere. During each scan line, the laser passes over the IDE annealing the LDCA that has been deposited (Figure 1e-g). This annealed film forms the active sensing layer, which has improved substrate adhesion. As the process proceeds excess material may overcoat the active layer, acting as a diffusion barrier to analytes, and must subsequently be removed to maximize device performance. This can be achieved by blowing pressurised air over the device once prepared (see Figure S6e). High magnification SEM reveals the annealed carbon aggregates, where the cluster size is approximately 20 nm (Figure 1f). Figure 1g and S7 show HRTEM image of the LDCA consisting of individual particulates in a non-crystalline mesostructure.

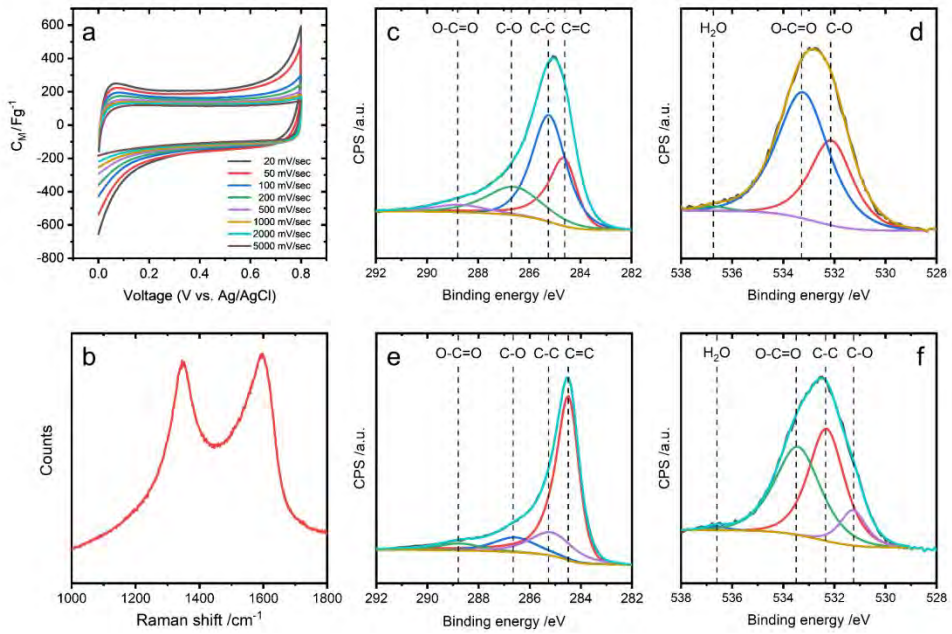

Fig2 a) Cyclic voltammographs at different cycling rates of active LDCA layer, b) Raman of annealed active LDCA layer c) Deconvoluted XPS spectra of C1-peak of diffusion barrier layer, d) Deconvoluted XPS spectra of O-peak of diffusion barrier layer, e) Deconvoluted XPS spectra of C1-peak of active LDCA layer f) Deconvoluted XPS spectra of O-peak of active LDCA layer.

To characterize the available surface area within the active LDCA the double layer capacitance was probed using cyclic voltammetry. The cyclic voltammographs (Figure 2a) show Faradaic reactions at the extrema with flat central regions, characteristic of non-Faradic double layer electrochemistry. At low scan rates the double layer capacitance is approximately 45 F/cm^3 which, due to only a fraction of the material being sp^2, corresponds to lower bound of the internal surface area per unit volume of $2.25 \cdot 10^6$ cm^2/cm^3 assuming a 20 $\mu F/cm^2$ theoretical capacitance for sp^2-hybridized carbon[22]. Interestingly, this is appreciably higher than soot or carbon black which can be up to 10^5 cm^2/cm^3 [23]. The layer thickness was estimated using an ellipsometer to be around 100 nm. Analysis of ellipsometry data can be found in Figure S8 with discussion of results in supporting information note 5.

Raman spectra (shown in Figure 2b) have characteristic D and G peaks, corresponding to defect and lattice modes respectively, with approximately equal intensity indicative of amorphous carbon[24]. XPS allows quantitative chemical analysis of the composition of the as-deposited and annealed LDCA material. Figure 2e indicates a high sp^2:sp^3 ratio for the annealed LDCA (around 62 at.% sp^2), greater than that for the as-deposited LDCA (around 22 at.% sp^2), shown in Figure 2c, despite their comparable C/O ratio of around 5. In addition, the presence of oxygen functional groups and adsorbed water on the surface is reduced after annealing (Figure 2f), suggesting some functionalization of the surface despite the increase in sp^2 character. Together, these measurements indicate that annealed LDCA comprises significant sp^2 carbon domains contained within functionalized shells.

Figure 3a shows the material’s response to concentrations

between 50 ppb and 1 ppm of NO_2 in a humid air environment. The

response amplitude increases with increasing NO_2 concentration

and saturates after an initial rise. Figure 3b depicts the

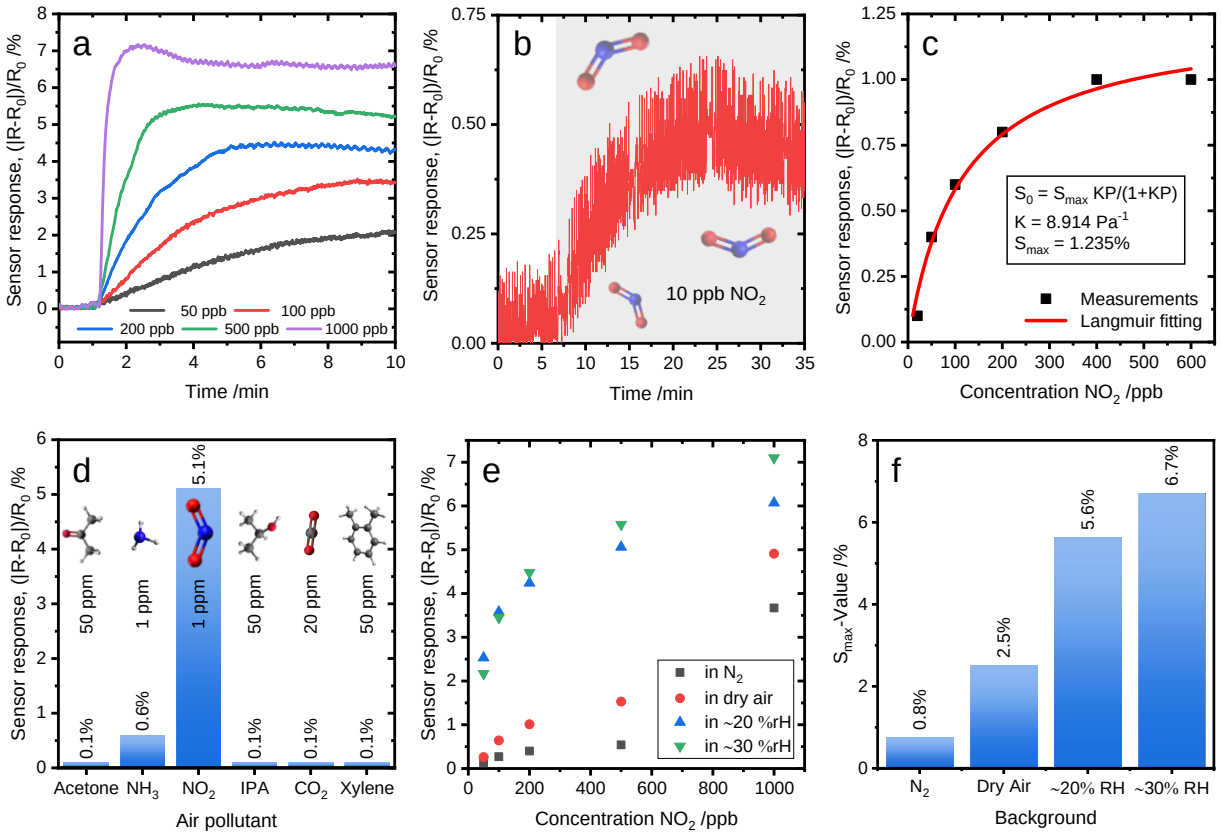

Fig3 a) Exposure to various concentrations from 50 ppb to 1000 ppb NO_2 in humid air environment (30 %RH), b)) single exposure to 10 ppb NO_2 in dry air, c) calibration curve with a Langmuir fitting in dry air showing surface adsorption behavior, d) selectivity measurements using NO_2, NH3 and various VOCs, a concentration of 1 ppm of NO_2 (in dry air) and NH_3 (in dry air), a concentration of 20 ppm of CO2 (in 20%RH) and 50 ppm of acetone, IPA and xylene was used for the measurement (all in 30% RH), e) NO2 calibration curve measurement in different backgrounds, f) S_{max}-values derived from Langmuir calibration curves fitted to the different background measurements.

measurement of a chemiresistor exposed to a 10 ppb of NO_2 in dry

air. A clear step is seen for this ultra-low concentration with adsorption times, t_{90}, the time it takes to reach 90% of the full amplitude, of around 10 min. The signal-to-noise ratio shown is relatively low and represents a threshold. However, this threshold is below the regulatory limit of 20ppb allowing for implementation in environmental sensors.

Figure 3c shows a response curve for the material as a function of concentration of NO_2 in dry air. The observed saturating behavior can be described using a Langmuir isotherm of the form $S_0 = S_{max}KP/(1+KP)$, where S_0 is the response, S_{max} is a constant, K is the equilibrium constant of the adsorption and desorption, and P is the partial pressure of the analyte. This model assumes surface adsorption/desorption of an analyte, and has been shown to apply well in the case of nanostructured materials[25]. The model is fitted to the data of Figure 3c in the low-concentration operating regime and accurately reproduces the observed trend, with a fitting constant S_{max} = 1.235 % and K = 8.914 Pa^{-1}. This calibration curve allows the readout of an exact concentration value. Figure 3d shows the response of the material towards different analytes at concentrations of 1 ppm of NH_3, 20 ppm of CO_2, 50 ppm of acetone, IPA and xylene respectively. Whereas NO_2 shows a strong response, the signals from NH_3 and other common VOCs are negligible, indicating a very high degree of selectivity towards NO^2. Figure 3e shows the

operation of the sensor in different background environments, including dry nitrogen, dry air, and at increasing humidity in air. The sensors have an elevated response in the presence of oxygen (dry air compared to N_2) and notably in a humid environment (30 %RH). Figure 3f shows the S_{max} values for the different backgrounds showing an increase with increasing humidity, which would require a humidity sensor to be incorporated in a fully realized device. For reference the removal of 400ppb NO_2, recovery of baseline by heating and re-exposure to 400ppb NO_2 is depicted in Figure S9. Due to humidity affecting sensitivity any device would require a humidity sensor to be run in parallel.

Typically, NO_2 detection by nanocarbon materials is commonly described via surface adsorption of gaseous NO_2 giving rise to charge transfer and an associated shift in the Fermi level of conjugated carbon nanomaterial[26]. This shift changes the conductivity[27], notably in graphene and nanotubes where the

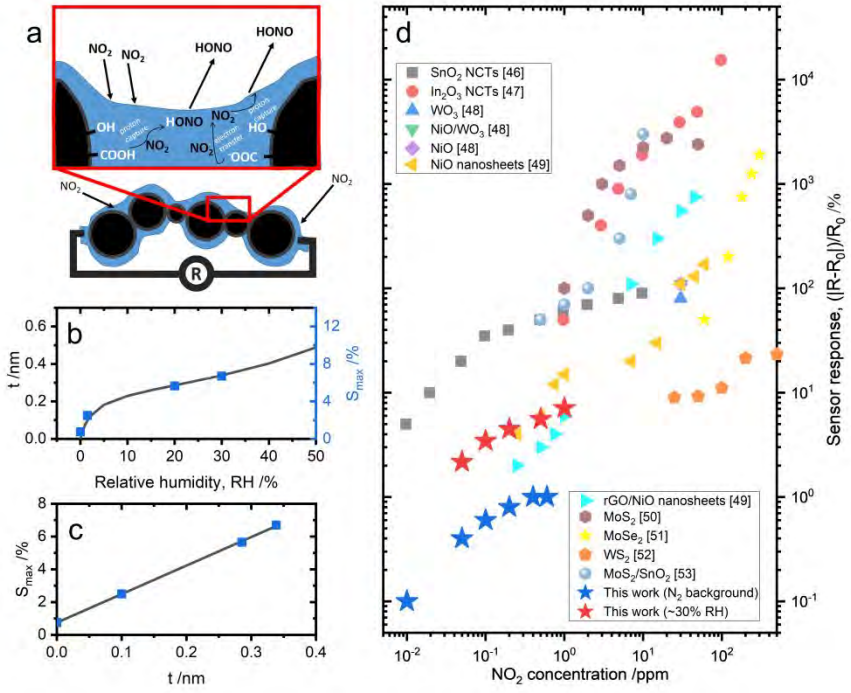

Fig4 a) Schematic showing the carbon particles with surface water layer and bridging water, with example reactions as NO_2 interacts with the water and organic carbon. R is the external resistance measurement which is primarily governed by the resistance of the water bridging the particles, b) Calculated BET isotherm showing the thickness of the adsorbed water layer against humidity, plotted alongside the sensitivity metric S_{max}, c) Plot of S_{max} vs adsorbed water layer thickness t, illustrating a robust linear trend, d) NO_2 calibration curves of various materials measured at room temperature.

density of states near to the Fermi level is very low. NO_2 binding is shown to be stronger in the presence of pre-existing defects in the carbon[28], such as at nanosheet edges in graphene films[29] or more readily on the surfaces of materials functionalized to improve their sensitivity and/or selectivity[30]. However, such a single mechanism does not account for the strong variation of sensitivity with atmospheric humidity (Figure 3e) even in the situation where there is competitive adsorption of both analyte and water molecules.

We propose an additional mechanism, shown in Figure 4a, which closely relates to known reactions in soot chemistry[14–17].This additional sensing mechanism can be understood based on the structure of the sensing layer (Figure 1g). It consists of a low-density array of carbon particles, very reminiscent of oxygen-poor soots (see Figure S10b,c). The XPS data suggests that after laser irradiation the particle surfaces and intermediate low-conductivity soot are functionalized with oxygen-containing species such as carboxyl groups. The material will therefore be highly hydrophilic and unless carefully excluded through appropriate heating and drying, a surface water layer will be present.

When this network of carbonaceous particles is weakly connected or below a percolation threshold, its overall conductivity will be mediated by conduction through the surface water layer, which

acts as a bridge between nearby particles. Thus, material conductivity will be strongly dependent on the conductivity through the water bridges, which in turn will strongly depend on ion content in the water.

As NO_2 dissolves in the water layer, interaction with the carbon surface chemistry results in ion formation in solution[14,16,31,32]. Such reactions are responsible for the selectivity of LDCA for NO_2. While the intrinsic water solubility of NO_2 is low[31], in the presence of carbonaceous species this changes whereby dissolved NO_2 reacts with soot particles to form nitrous acid HONO[16]. These acid species result in soluble ions such as NO_2^- and NO_4^- and can result in significant NO_2 take-up . The material is thus responding to, via resistance change, the ion concentration in the electrode surface water layer, and indirectly therefore, the NO_2 breakdown process of the carbon layer. The material can then measure, via resistance change, the ion concentration in the electrode surface water layer, and indirectly therefore, the NO_2 breakdown process of the carbon layer. We note that the importance of the water layer can be demonstrated by freezing; operating at -25°C decreases the sensor response to 1ppm NO_2 by an order of magnitude as compared to room temperature. The presence of charged oxygen in water, an additional result of soot chemistry, can result in charge exchange between solvated NO_2 and O_2^- [33–35]. This explains the

difference in sensitivity of the sensor in the dry air environment compared to the dry N_2 environment shown in figure 3e.

As mentioned above, oxidized soot particles are also known to have carboxylated surfaces[36] which can interact strongly with water vapour[37], notably in atmospheric chemistry where they can act as cloud nuclei[36]. As such, we tested the above theory through production of a similar chemiresistor fabricated using propane soot, which indeed shows NO_2 detection, albeit at lower sensitivity (presumably due to less optimal structure and porosity, see Figure S11). We note that this mechanism also explains why there is higher sensitivity to NO_2 than NH_3 and CO_2. While NH_3 has extremely high solubility in water it will rapidly form ionic dielectric shells around opposing exposed carbon surfaces in the electrode, and hence, while there will be a strong initial capacitive response, there is no subsequent electrolytic response or mechanism for continuous ion transfer[38]. Similarly, for CO_2, the solubility and conversion to carbonic acid results in negligible ion generation due to its weak acid character. In contrast conduction with NO_2 is mediated through continuous reaction with the carbonaceous electrode. The other reactants are either insoluble in water or do not form any ions in solution.

To understand the apparent increasing sensitivity (indicated by the value of S_{max}) as a function of humidity, we use the BET isotherm (calculation outlined in Supplementary Note 6) to evaluate the changing thickness of the adsorbed water layer on the LDCA. Figure 4b compares the resulting calculated water layer thickness with the fitted S_{max} values as a function of relative humidity and points to a clear correlation between the two. This correlation is further evidenced in Figure 4c where S_{max} is plotted as a function of water layer thickness and fitted to a simple linear regression. Interestingly, the intercept of regression is non-zero. Clearly, there is both sensitivity at zero humidity (corresponding to the sensor measurements performed in dry nitrogen) and an increase in sensitivity with adsorbed thickness of the water layer lending support to the hypothesized mechanism based on dissolution of NO_2 within the adsorbed water layer. We note that if dissolution within the water layer was solely responsible for the sensing response, we should expect there to be no analyte response in the absence of an adsorbed water layer. Although the presence of chemisorbed water cannot be discounted, this may infer that, at very low values of humidity, there is potentially a second sensing mechanism contributing to the overall response based on direct adsorption of NO_2[39].

This mechanism presented accounts for the sensitivity, selectivity and humidity dependence of this LDCA material, justifying its impressive performance and potential to be competitive with existing room-temperature NO_2 sensing materials. A comparison of response versus NO_2 concentration for a range of room temperature operation metal oxides, graphene materials and transition metal dichalcogenides (TMDs) is shown in Figure 4d. This illustrates that ppb NO_2 sensing has not yet been demonstrated with TMDs, despite their appreciable sensor response, and graphene-based materials must be combined with metal oxides in order to combine sensitivity and low limit of detection. Metal oxides, particularly SnO_2, are the only materials which have been shown to allow ppb NO_2 sensing, highlighting LDCA as a disruptor technology alternative which can be produced by a low-cost scalable processing. While the sensitivity (in terms of resistance change) of LDCA is lower than most metal oxides, their competitive performance at this early stage of development emphasizes its potential for low limit detection of NO_2 in a highly selective manner. This low limit of detection is attributed to the high surface area of the material, the conductivity of the material, and the specificity of the mechanism. The unidirectionality of the NO_2 solubilization allows the water layer to accumulate more ions over time which allows effective sensing of the low ppb concentrations due to

this unique sensing mechanism. It is possible that fluctuations in the baseline conductivity of semiconductor sensors make low limit of detection analysis more challenging, hence the lack of reported ppb semiconductor and oxide NO_2 sensors.

Conclusions

In summary, a thin, porous and well adhered film of LDCA is deposited in a cheap but scalable single-step laser process on readout electrodes to form a chemiresistor structure for possible application in distributed air quality monitoring. Exposure to NO_2 shows a detection limit below 10 ppb and response times below 15 min, facilitating simple measurements of NO_2 pollution in air in compliance with EU regulations. These as-produced LDCAs show exceptional selectivity towards NO_2 over other common air pollutants making them unique amongst carbon nanomaterials[4,9,30,40–43]. The sensors perform better in a humid environment making them readily applicable for real world measurements. A novel sensing mechanism is proposed based on NO_2 solubility and reactivity in sensor surface water layers. A comparison of the performance of various materials for NO_2 gas sensing (Figure 4d) shows that with this work the carbon based materials can reach or exceed the current limit of detection values of other state-of-the-art materials, when operated at room-temperature[44,45]. Room-temperature operation is crucial to

reduce power consumption so that the material can be incorporated into routine continuous air quality monitoring Internet-of-Things devices and applications.

Corresponding Author

*University of Sussex, Department of Physics and Astronomy, Brighton, BN1 9RH, UK, A.B.Dalton@sussex.ac.uk

*Institute des Matériaux Jean Rouxel (IMN), CNRS UMR6502 / Université de Nantes, Nantes, 44322, France, Chris.Ewels@cnrs-imn.fr

Present Addresses

†SENSIRION AG, Laubisruetistrasse 50, CH-8712 Staefa ZH, Switzerland

Author Contributions

S.N. performed development and fabrication of samples, devices and the gas measurements. C.E. and N.T. analysed the sensing mechanism. P.L. performed the cyclic voltammetry measurements. S.N., M.L, S.O., A.D., C.E. and P.L. were responsible for the preparation of the manuscript. E.M., M.P., R.A. were responsible for the TEM images taken. J.S. was responsible for the collection of the SEM data. W.K.M.

and A.M.B. prepared the graphene oxide sample and analyzed the XPS data. A.B and A.D. were responsible for the overall direction of the project.

Funding Sources

Notes

The authors declare no competing interests

ACKNOWLEDGMENTS

This project has received funding from the European Union's Horizon 2020 research and innovation program under the Marie Sklodowska-Curie Grant agreement No 642742.

ABBREVIATIONS

LDCA, Laser deposited carbon aerogel; ITO, Indium Tin Oxide; IDE, Inter-digitated electrode

REFERENCES

(1) Orehek, J.; Massari, J. P.; Gayrard, P.; Grimaud, C.; Charpin, J. Effect of Short-Term, Low-Level Nitrogen Dioxide Exposure on Bronchial Sensitivity of Asthmatic Patients. *The Journal of clinical investigation* **1976**, *57* (2), 301–7.

(2) Aguilera, I.; Pedersen, M.; Garcia-Esteban, R.; Ballester, F.; Basterrechea, M.; Esplugues, A.; Fernández-Somoano, A.; Lertxundi, A.; Tardón, A.; Sunyer, J. Early-Life Exposure to Outdoor Air Pollution and Respiratory Health, Ear Infections, and Eczema in Infants from the INMA Study. *Environmental health perspectives* **2013**, *121* (3), 387–92. https://doi.org/10.1289/ehp.1205281.

(3) Agency, E. Performance Standards for Continous Ambient Air Quality Monitoring Systems. *www.gov.uk* **2016**.

(4) Melios, C.; Panchal, V.; Edmonds, K.; Lartsev, A.; Yakimova, R.; Kazakova, O. Detection of Ultralow Concentration NO2 in Complex Environment Using Epitaxial Graphene Sensors. *ACS Sensors* **2018**, *3* (9), 1666–1674.

(5) Marshall, C. Air Pollution Linked to Child's Death. *BBC News*. July 3, 2018.

(6) Liu, X.; Cheng, S.; Liu, H.; Hu, S.; Zhang, D.; Ning, H. A Survey on Gas Sensing Technology. *Sensors* **2012**, *12* (7), 9635–9665.

(7) Apte, J. S.; Messier, K. P.; Gani, S.; Brauer, M.; Kirchstetter, T. W.; Lunden, M. M.; Marshall, J. D.; Portier, C. J.; Vermeulen, R. C.; Hamburg, S. P. High-Resolution Air Pollution Mapping with Google Street View Cars: Exploiting Big Data. *Environmental Science & Technology* **2017**, *51* (12), 6999–7008.

(8) Zhang, Z.; Wen, Z.; Ye, Z.; Zhu, L. Ultrasensitive Ppb-Level NO2 Gas Sensor Based on WO3 Hollow Nanosphers Doped with Fe. *Applied Surface Science* **2018**, *434*, 891–897.

(9) Llobet, E. Gas Sensors Using Carbon Nanomaterials: A Review. *Sensors and Actuators B: Chemical* **2013**, *179*, 32–45.

(10) Valentini, L.; Armentano, I.; Kenny, J.; Cantalini, C.; Lozzi, L.; Santucci, S. Sensors for Sub-Ppm NO2 Gas Detection Based on Carbon Nanotube Thin Films. *Applied Physics Letters* **2003**, *82* (6), 961–963.

(11) Qi, P.; Vermesh, O.; Grecu, M.; Javey, A.; Wang, Q.; Dai, H.; Peng, S.; Cho, K. Toward Large Arrays of Multiplex Functionalized Carbon Nanotube Sensors for Highly Sensitive and Selective Molecular Detection. *Nano Letters* **2003**, *3* (3), 347–351.

(12) Chung, M. G.; Kim, D. H.; Lee, H. M.; Kim, T.; Choi, J. H.; kyun Seo, D.; Yoo, J.-B.; Hong, S.-H.; Kang, T. J.; Kim, Y. H. Highly Sensitive NO2 Gas Sensor Based on Ozone Treated Graphene. *Sensors and Actuators B: Chemical* **2012**, *166*, 172–176.

(13) Nufer, S.; Fantanas, D.; Ogilvie, S. P.; Large, M. J.; Winterauer, D. J.; Salvage, J. P.; Meloni, M.; King, A. A.; Schellenberger, P.; Shmeliov, A.; others. Percolating Metallic Structures Templated on Laser-Deposited Carbon Nanofoams Derived from Graphene Oxide: Applications in Humidity Sensing. *ACS Applied Nano Materials* **2018**, *1* (4), 1828–1835.

(14) Lahoutifard, N.; Ammann, M.; Gutzwiller, L.; Ervens, B.; George, C. The Impact of Multiphase Reactions of NO 2 with Aromatics: A Modelling Approach. *Atmospheric Chemistry and Physics* **2002**, *2* (3), 215–226.

(15) Leistner, K. *Experimental and Modelling Study of Catalytic Diesel Soot Oxidation*; Université Pierre et Marie Curie-Paris VI, 2012.

(16) Han, C.; Liu, Y.; He, H. Role of Organic Carbon in Heterogeneous Reaction of NO2 with Soot. *Environmental science & technology* **2013**, *47* (7), 3174–81. https://doi.org/10.1021/es304468n.

(17) Monge, M. E.; D'Anna, B.; Mazri, L.; Giroir-Fendler, A.; Ammann, M.; Donaldson, D. J.; George, C. Light Changes the Atmospheric Reactivity of Soot. *Proceedings of the National Academy of Sciences of the United States of America* **2010**, *107* (15), 6605–9. https://doi.org/10.1073/pnas.0908341107.

(18) Henley, S.; Carey, J.; Silva, S.; Fuge, G.; Ashfold, M.; Anglos, D. Dynamics of Confined Plumes during Short and Ultrashort Pulsed Laser Ablation of Graphite. *Physical Review B* **2005**, *72* (20), 205413.

(19) Rode, A. V.; Hyde, S.; Gamaly, E.; Elliman, R.; McKenzie, D.; Bulcock, S. Structural Analysis of a Carbon Foam Formed by High Pulse-Rate Laser Ablation. *Applied Physics A: Materials Science & Processing* **1999**, *69* (7), S755–S758.

(20) Rode, A. V.; Gamaly, E. G.; Luther-Davies, B. Formation of Cluster-Assembled Carbon Nano-Foam by High-Repetition-Rate Laser Ablation. *Applied Physics A: Materials Science & Processing* **2000**, *70* (2), 135–144.

(21) Nufer, S.; Lynch, P.; Cann, M.; Large, M. J.; Salvage, J. P.; Víctor-Román, S.; Hernández-Ferrer, J.; Benito, A. M.; Maser, W. K.; Brunton, A.; others. Carbon Nanofoam Supercapacitor Electrodes with Enhanced Performance Using a Water-Transfer Process. *ACS Omega* **2018**, *3* (11), 15134–15139.

(22) Xia, J.; Chen, F.; Li, J.; Tao, N. Measurement of the Quantum Capacitance of Graphene. *Nature nanotechnology* **2009**, *4* (8), 505–9. https://doi.org/10.1038/nnano.2009.177.

(23) Harris, S. J.; Weiner, A. M. Chemical Kinetics of Soot Particle Growth. *Annual Review of Physical Chemistry* **1985**, *36* (1), 31–52.
(24) Ferrari, A. C.; Robertson, J. Interpretation of Raman Spectra of Disordered and Amorphous Carbon. *Physical review B* **2000**, *61* (20), 14095.
(25) Kohrt, C.; Gomer, R. Adsorption of CO on the (110) Plane of Tungsten; Temperature Dependence of the Sticking Coefficient and Absolute Surface Coverages. *Surface Science* **1973**, *40* (1), 71–84.
(26) Ghouma, I.; Jeguirim, M.; Limousy, L.; Bader, N.; Ouederni, A.; Bennici, S. Factors Influencing NO2 Adsorption/Reduction on Microporous Activated Carbon: Porosity vs. Surface Chemistry. *Materials* **2018**, *11* (4), 622.
(27) Kong, J.; Franklin, N. R.; Zhou, C.; Chapline, M. G.; Peng, S.; Cho, K.; Dai, H. Nanotube Molecular Wires as Chemical Sensors. *Science* **2000**, *287* (5453), 622–625.
(28) Liu, Y.; Liu, H.; Chu, Y.; Cui, Y.; Hayasaka, T.; Dasaka, V.; Nguyen, L.; Lin, L. Defect-Induced Gas Adsorption on Graphene Transistors. *Advanced Materials Interfaces* **2018**, *5* (9), 1701640.
(29) Nufer, S.; Large, M. J.; King, A. A.; Ogilvie, S. P.; Brunton, A.; Dalton, A. B. Edge Selective Gas Detection Using Langmuir Films of Graphene Platelets. *ACS applied materials & interfaces* **2018**, *10* (25), 21740–21745.
(30) Varghese, S. S.; Lonkar, S.; Singh, K.; Swaminathan, S.; Abdala, A. Recent Advances in Graphene Based Gas Sensors. *Sensors and Actuators B: Chemical* **2015**, *218*, 160–183.
(31) Schwartz, S.; White, W. *Solubility Equilibria of the Nitrogen Oxides and Oxyacids in Dilute Aqueous Solution*; science, A. in environmental, engineering., Eds.; Gordon and Breach Science Publishers, 1981; Vol. 4.
(32) Sweeney, A. J.; Liu, Y. Use of Simulation to Optimize NO x Abatement by Absorption and Selective Catalytic Reduction. *Industrial & engineering chemistry research* **2001**, *40* (12), 2618–2627.
(33) Mendiara, T.; Alzueta, M. U.; Millera, A.; Bilbao, R. Influence of the NO Concentration and the Presence of Oxygen in the Acetylene Soot Reaction with NO. *Energy Fuels* **2008**, *22* (1), 284–290. https://doi.org/10.1021/ef700580t.
(34) Suzuki, T.; Kyotani, T.; Tomita, A. Study on the Carbon-Nitric Oxide Reaction in the Presence of Oxygen. *Ind. Eng. Chem. Res.* **1994**, *33* (11), 2840–2845. https://doi.org/10.1021/ie00035a038.
(35) Stanmore, B. R.; Tschamber, V.; Brilhac, J.-F. Oxidation of Carbon by NOx, with Particular Reference to NO2 and N2O. *Fuel* **2008**, *87* (2), 131–146. https://doi.org/10.1016/j.fuel.2007.04.012.
(36) Decesari, S.; Facchini, M.; Matta, E.; Mircea, M.; Fuzzi, S.; Chughtai, A.; Smith, D. Water Soluble Organic Compounds Formed by Oxidation of Soot. *Atmospheric Environment* **2002**, *36* (11), 1827–1832.
(37) Weingartner, E.; Burtscher, H.; Baltensperger, U. Hygroscopic Properties of Carbon and Diesel Soot Particles. *Atmospheric Environment* **1997**, *31* (15), 2311–2327.
(38) Koh, A. R.; Hwang, B.; Roh, K. C.; Kim, K. The Effect of the Ionic Size of Small Quaternary Ammonium BF 4 Salts on Electrochemical Double Layer Capacitors. *Physical Chemistry Chemical Physics* **2014**, *16* (29), 15146–15151.
(39) Lee, S. W.; Lee, W.; Hong, Y.; Lee, G.; Yoon, D. S. Recent Advances in Carbon Material-Based NO2 Gas Sensors. *Sensors and Actuators B: Chemical* **2018**, *255*, 1788–1804.
(40) Schedin, F.; Geim, A. K.; Morozov, S. V.; Hill, E. W.; Blake, P.; Katsnelson, M. I.; Novoselov, K. S. Detection of Individual Gas Molecules Adsorbed on Graphene. *Nature materials* **2007**, *6* (9), 652–5.
(41) Li, J.; Lu, Y. J.; Ye, Q.; Cinke, M.; Han, J.; Meyyappan, M. Carbon Nanotube Sensors for Gas and Organic Vapor Detection. *Nano Letters* **2003**, *3* (7), 929–933. https://doi.org/10.1021/nl034220x.
(42) Lin, H.-B.; Shih, J.-S. Fullerene C60-Cryptand Coated Surface Acoustic Wave Quartz Crystal Sensor for Organic Vapors. *Sensors and Actuators B: Chemical* **2003**, *92* (3), 243–254.

(43) Yavari, F.; Chen, Z.; Thomas, A. V.; Ren, W.; Cheng, H.-M.; Koratkar, N. High Sensitivity Gas Detection Using a Macroscopic Three-Dimensional Graphene Foam Network. *Scientific reports* **2011**, *1*, 166.

(44) Zhang, C.; Luo, Y.; Xu, J.; Debliquy, M. Room Temperature Conductive Type Metal Oxide Semiconductor Gas Sensors for NO2 Detection. *Sensors and Actuators A: Physical* **2019**, *289*, 118–133.

(45) Joshi, N.; Hayasaka, T.; Liu, Y.; Liu, H.; Oliveira, O. N.; Lin, L. A Review on Chemiresistive Room Temperature Gas Sensors Based on Metal Oxide Nanostructures, Graphene and 2D Transition Metal Dichalcogenides. *Microchimica Acta* **2018**, *185* (4), 213.

(46) Jiang, C.; Zhang, G.; Wu, Y.; Li, L.; Shi, K. Facile Synthesis of SnO2 Nanocrystalline Tubes by Electrospinning and Their Fast Response and High Sensitivity to NOx at Room Temperature. *CrystEngComm* **2012**, *14* (8), 2739–2747. https://doi.org/10.1039/C2CE06405G.

(47) Gao, J.; Wu, H.; Zhou, J.; Yao, L.; Zhang, G.; Xu, S.; Xie, Y.; Li, L.; Shi, K. Mesoporous In2O3 Nanocrystals: Synthesis, Characterization and NOx Gas Sensor at Room Temperature. *New J. Chem.* **2016**, *40* (2), 1306–1311. https://doi.org/10.1039/C5NJ02214B.

(48) Bao, M.; Chen, Y.; Li, F.; Ma, J.; Lv, T.; Tang, Y.; Chen, L.; Xu, Z.; Wang, T. Plate-like p–n Heterogeneous NiO/WO3 Nanocomposites for High Performance Room Temperature NO2 Sensors. *Nanoscale* **2014**, *6* (8), 4063–4066. https://doi.org/10.1039/C3NR05268K.

(49) Zhang, J.; Zeng, D.; Zhao, S.; Wu, J.; Xu, K.; Zhu, Q.; Zhang, G.; Xie, C. Room Temperature NO2 Sensing: What Advantage Does the RGO-NiO Nanocomposite Have over Pristine NiO? *Phys Chem Chem Phys* **2015**, *17* (22), 14903–14911. https://doi.org/10.1039/c5cp01987g.

(50) Cho, B.; Hahm, M. G.; Choi, M.; Yoon, J.; Kim, A. R.; Lee, Y.-J.; Park, S.-G.; Kwon, J.-D.; Kim, C. S.; Song, M.; Jeong, Y.; Nam, K.-S.; Lee, S.; Yoo, T. J.; Kang, C. G.; Lee, B. H.; Ko, H. C.; Ajayan, P. M.; Kim, D.-H. Charge-Transfer-Based Gas Sensing Using Atomic-Layer MoS 2. *Scientific Reports* **2015**, *5* (1), 8052. https://doi.org/10.1038/srep08052.

(51) Baek, J.; Yin, D.; Liu, N.; Omkaram, I.; Jung, C.; Im, H.; Hong, S.; Kim, S. M.; Hong, Y. K.; Hur, J.; Yoon, Y.; Kim, S. A Highly Sensitive Chemical Gas Detecting Transistor Based on Highly Crystalline CVD-Grown MoSe2 Films. *Nano Res.* **2017**, *10* (6), 1861–1871. https://doi.org/10.1007/s12274-016-1291-7.

(52) Ko, K. Y.; Song, J.-G.; Kim, Y.; Choi, T.; Shin, S.; Lee, C. W.; Lee, K.; Koo, J.; Lee, H.; Kim, J.; Lee, T.; Park, J.; Kim, H. Improvement of Gas-Sensing Performance of Large-Area Tungsten Disulfide Nanosheets by Surface Functionalization. *ACS Nano* **2016**, *10* (10), 9287–9296. https://doi.org/10.1021/acsnano.6b03631.

(53) Cui, S.; Wen, Z.; Huang, X.; Chang, J.; Chen, J. Stabilizing MoS2 Nanosheets through SnO2 Nanocrystal Decoration for High-Performance Gas Sensing in Air. *Small* **2015**, *11* (19), 2305–2313. https://doi.org/10.1002/smll.201402923.